IEEE TRANSACTIONS ON

GEOSCIENCE AND REMOTE SENSING

A PUBLICATION OF THE IEEE GEOSCIENCE AND REMOTE SENSING SOCIETY

MAY 2016 VOLUME 54 NUMBER 5 IGRSD2 (ISSN 0196-2892)

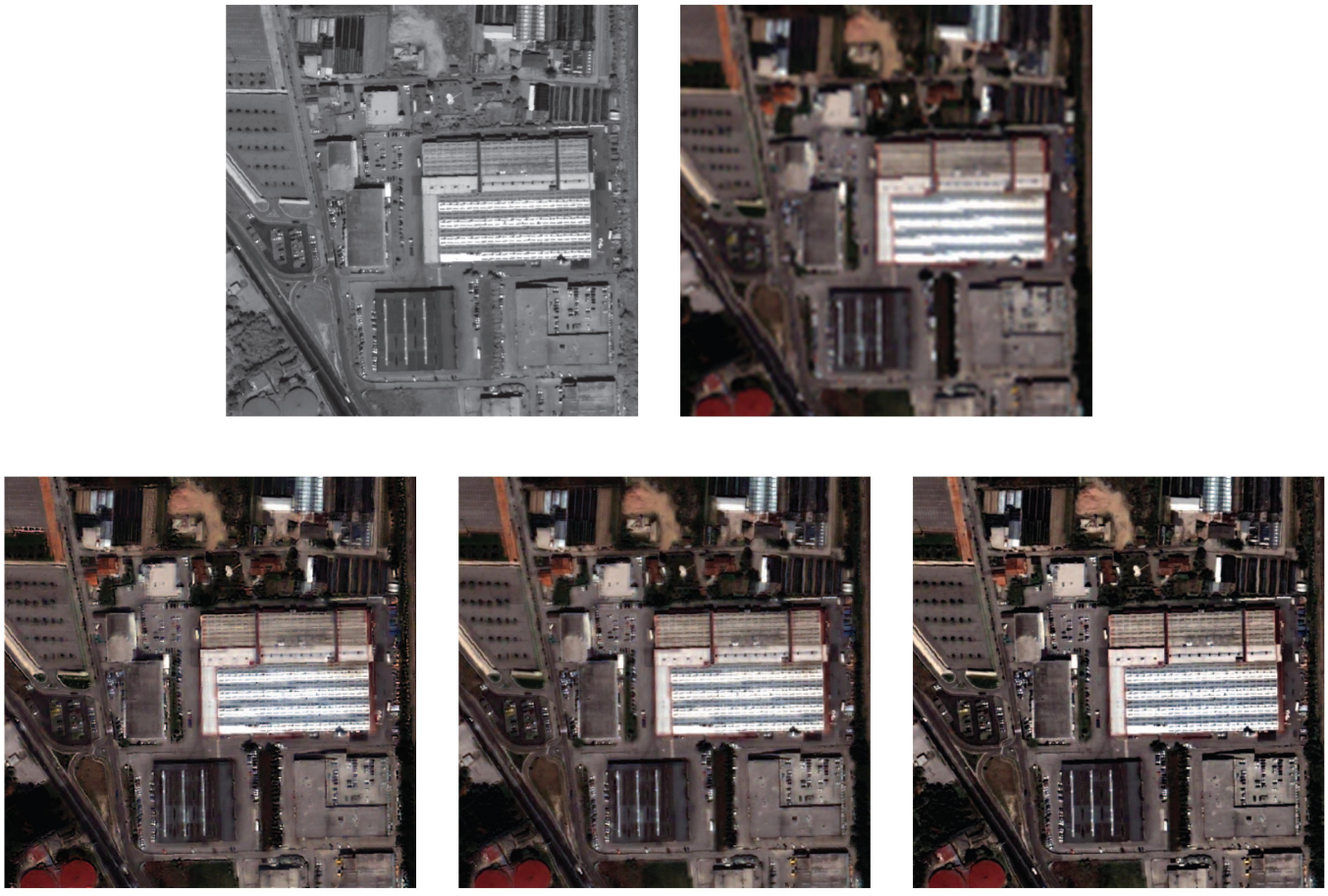

QuickBird image: True-color (top right) and panchromatic (top left) at 0.7-m scale. Pansharpened products: generalized Laplacian pyramid (bottom left) and "á trous" wavelet transform (bottom middle), both with spatial optimization to the modulation transfer function of the system. Adaptive Gram–Schmidt with spectral optimization achieved through multivariate regression (bottom right).

IEEE TRANSACTIONS ON

GEOSCIENCE AND REMOTE SENSING

A PUBLICATION OF THE IEEE GEOSCIENCE AND REMOTE SENSING SOCIETY

MAY 2016 VOLUME 54 NUMBER 5 IGRSD2 (ISSN 0196-2892)

PAPERS

Atmosphere

Reconstruction of Fine-Scale Auroral Dynamics . . . . . *M. Hirsch, J. Semeter, M. Zettergren, H. Dahlgren, C. Goenka, and H. Akbari* 2780

Multimodel Prediction of Monsoon Rain Using Dynamical Model Selection . . . . . *S. Bhomia, N. Jaiswal, C. M. Kishtawal, and R. Kumar* 2911

Cryosphere

Ground-Based Water Vapor Retrieval in Antarctica: An Assessment . . . . . *M. Negusini, B. H. Petkov, P. Sarti, and C. Tomasi* 2935

Vegetation and Land

Measurement and Analysis of Bidirectional SIF Emissions in Wheat Canopies . . . . . *L. Liu, X. Liu, Z. Wang, and B. Zhang* 2640

Subsurface and Geology

Time-Gating-Based Time Reversal Imaging for Impulse Borehole Radar in Layered Media . . . . . *H. Yang, T. Li, N. Li, Z. He, and Q. H. Liu* 2695

Hyperspectral Data Processing

A Web-Based Tool for Calculating Spectral Band Difference Adjustment Factors Derived From SCIAMACHY Hyperspectral Data . . . . . *B. R. Scarino, D. R. Doelling, P. Minnis, A. Gopalan, T. Chee, R. Bhatt, C. Lukashin, and C. Haney* 2529

Nonnegative Tensor CP Decomposition of Hyperspectral Data . . . . . *M. A. Veganzones, J. E. Cohen, R. Cabral Farias, J. Chanussot, and P. Comon* 2577

Kernel-Based Domain-Invariant Feature Selection in Hyperspectral Images for Transfer Learning . . . . . *C. Persello and L. Bruzzone* 2615

Hyperspectral Image Analysis by Spectral–Spatial Processing and Anticipative Hybrid Extreme Rotation Forest Classification . . . . . *B. Ayerdi and M. Graña Romay* 2627

Unsupervised Multitemporal Spectral Unmixing for Detecting Multiple Changes in Hyperspectral Images . . . . . *S. Liu, L. Bruzzone, F. Bovolo, and P. Du* 2733

(Contents Continued on Page 2494)

(Contents Continued from Page 2493)

A Novel Spectral Unmixing Method Incorporating Spectral Variability Within Endmember Classes . . . . . T. Uezato, R. J. Murphy, A. Melkumyan, and A. Chlingaryan 2812
Two-Step Constrained Nonlinear Spectral Mixture Analysis Method for Mitigating the Collinearity Effect . . . . . L. Ma, J. Chen, Y. Zhou, and X. Chen 2873
Cloud Removal Based on Sparse Representation via Multitemporal Dictionary Learning . . . . . M. Xu, X. Jia, M. Pickering, and A. J. Plaza 2998

Image Processing and Analysis

Spatial Methods for Multispectral Pansharpening: Multiresolution Analysis Demystified . . . . . L. Alparone, S. Baronti, B. Aiazzi, and A. Garzelli 2563
Exploiting Joint Sparsity for Pansharpening: The J-SparseFI Algorithm . . . . . X. X. Zhu, C. Grohnfeldt, and R. Bamler 2664
An Iterative Haze Optimized Transformation for Automatic Cloud/Haze Detection of Landsat Imagery . . . . . S. Chen, X. Chen, J. Chen, P. Jia, X. Cao, and C. Liu 2682
Detection and Correction of Glitches in a Multiplexed Multichannel Data Stream—Application to the MADRAS Instrument . . . . . H. Wendt, N. Dobigeon, J.-Y. Tourneret, M. Albinet, C. Goldstein, and N. Karouche 2803
Adaptive Sparse Subpixel Mapping With a Total Variation Model for Remote Sensing Imagery . . . . . R. Feng, Y. Zhong, X. Xu, and L. Zhang 2855
Stripe Noise Separation and Removal in Remote Sensing Images by Consideration of the Global Sparsity and Local Variational Properties . . . . . X. Liu, X. Lu, H. Shen, Q. Yuan, Y. Jiao, and L. Zhang 3049
Multiple Morphological Component Analysis Based Decomposition for Remote Sensing Image Classification . . . . . X. Xu, J. Li, X. Huang, M. Dalla Mura, and A. Plaza 3083

Microwave Radiometry

Improving Multiyear Ice Concentration Estimates With Reanalysis Air Temperatures . . . . . Y. Ye, G. Heygster, and M. Shokr 2602
Optimum Image Formation for Spaceborne Microwave Radiometer Products . . . . . D. G. Long and M. J. Brodzik 2763
Global Sensitivity Analysis of the L-MEB Model for Retrieving Soil Moisture . . . . . Z. Wang, T. Che, and Y.-A. Liou 2949

Radar Systems

Enhanced-Resolution Reconstruction of ASCAT Backscatter Measurements . . . . . R. D. Lindsley and D. G. Long 2589
Semiparametric Algorithm for Processing MST Radar Data . . . . . N. I. Eappen, T. S. Reddy, and G. R. Reddy 2713
Performance Analysis of Incoherent RF Tomography Using Wireless Sensor Networks . . . . . G. Gennarelli and F. Soldovieri 2722
Information-Theoretic Feature Selection for Human Micro-Doppler Signature Classification . . . . . B. Tekeli, S. Z. Gurbuz, and M. Yuksel 2749
Calibration and Validation of the RapidScat Scatterometer Using Tropical Rainforests . . . . . N. M. Madsen and D. G. Long 2846
Mitigation of Wind Turbine Clutter for Weather Radar by Signal Separation . . . . . F. Uysal, I. Selesnick, and B. M. Isom 2925
An Improved Attributed Scattering Model Optimized by Incremental Sparse Bayesian Learning . . . . . Z. Li, K. Jin, B. Xu, W. Zhou, and J. Yang 2973
Surface Current Measurements Using X-Band Marine Radar With Vertical Polarization . . . . . W. Huang, R. Carrasco, C. Shen, E. W. Gill, and J. Horstmann 2988

Synthetic Aperture Radar

An Integrated Surface Parameter Inversion Scheme Over Agricultural Fields at Early Growing Stages by Means of C-Band Polarimetric RADARSAT-2 Imagery . . . . . X. Huang, J. Wang, and J. Shang 2510
Coupled Model Simulation of Wind Stress Effect on Far Wakes of Ships in SAR Images . . . . . A. Fujimura, A. Soloviev, S. H. Rhee, and R. Romeiser 2543
Fast Backprojection Algorithms Based on Subapertures and Local Polar Coordinates for General Bistatic Airborne SAR Systems . . . . . V. T. Vu and M. I. Pettersson 2706
Extended Three-Stage Polarimetric SAR Interferometry Algorithm by Dual-Polarization Data . . . . . F. Wenxue, G. Huadong, L. Xinwu, T. Bangsen, and S. Zhongchang 2792
Single and Multipolarimetric P-Band SAR Tomography of Subsurface Ice Structure . . . . . F. Banda, J. Dall, and S. Tebaldini 2832
A Segmentation-Based CFAR Detection Algorithm Using Truncated Statistics . . . . . D. Tao, A. P. Doulgeris, and C. Brekke 2887

(Contents Continued on Page 3104)

(Contents Continued from Page 2494)

Using an Integer Least Squares Estimator to Connect Isolated InSAR Fringes in Earthquake Slip Inversion . . . . . *C. Wang, X. Ding, Q. Li, X. Shan, and P. Liu* 2899
Determining the Points of Change in Time Series of Polarimetric SAR Data . . . . . *K. Conradsen, A. A. Nielsen, and H. Skriver* 3007
A SAR Image Despeckling Method Based on Two-Dimensional S Transform Shrinkage . . . . . *F. Gao, X. Xue, J. Sun, J. Wang, and Y. Zhang* 3025
A Physical Analysis of Polarimetric SAR Data Statistical Models . . . . *X. Deng, C. López-Martínez, and E. M. Varona* 3035
Influence of Vegetation Growth on the Polarimetric Zero-Baseline DInSAR Phase Diversity—Implications for Deformation Studies . . . . . *S. Zwieback and I. Hajnsek* 3070

Global Navigation Satellite System

Calibration and Unwrapping of the Normalized Scattering Cross Section for the Cyclone Global Navigation Satellite System . . . . . *S. Gleason, C. S. Ruf, M. P. Clarizia, and A. J. O'Brien* 2495
First Results of a GNSS-R Experiment From a Stratospheric Balloon Over Boreal Forests . . . . . *H. Carreno-Luengo, A. Camps, J. Querol, and G. Forte* 2652

UV/Visible/Infrared Imagers

Review of Thermal Infrared Applications and Requirements for Future High-Resolution Sensors . . . . . *J. A. Sobrino, F. Del Frate, M. Drusch, J. C. Jiménez-Muñoz, P. Manunta, and A. Regan* 2963
Test of the MODIS Land Surface Temperature and Emissivity Separation Algorithm With Ground Measurements Over a Rice Paddy . . . . . *C. Coll, V. García-Santos, R. Niclós, and V. Caselles* 3061

Satellite Systems

Kriging and Local Polynomial Methods for Blending Satellite-Derived and Gauge Precipitation Estimates to Support Hydrologic Early Warning Systems . . . . . *A. Verdin, C. Funk, B. Rajagopalan, and W. Kleiber* 2552
Assessment of SNPP VIIRS VIS/NIR Radiometric Calibration Stability Using Aqua MODIS and Invariant Surface Targets . . . . . *A. Wu, X. Xiong, C. Cao, and K.-F. Chiang* 2918

About the Cover: The cover figure shows original multispectral (MS) and panchromatic (P) images, acquired by the QuickBird satellite system on an industrial area near Trento, in Italy, and the pansharpened versions, achieved by means of two spatial and one spectral fusion methods. Both visual and numerical evidence demonstrate that the two classes of methods, once they have been optimized to match the respective spatial/spectral models of the instrument, produce very similar results, notwithstanding they follow totally different approaches. Optimization of spatial methods is achieved by designing a parametric lowpass filter matching the Modulation Transfer Function (MTF) of the MS instrument. A unique filter, and not a filter bank, rules the behavior of spatial methods, traditionally contextualized within multiresolution analysis. Optimization of spectral methods is achieved by means of a multivariate regression of the original MS bands to a spatially degraded version of the P image. For more information please see ''Spatial methods for Multispectral Pansharpening: Multiresolution Analysis Demystified,'' by Alparone *et al.*, which begins on page 2563.